Journal of Colloid and Interface Science 701 (2026) 138664

Contents lists available at ScienceDirect

Journal of Colloid And Interface Science

journal homepage: www.elsevier.com/locate/jcis

# Trimesic acid modified copper-cobalt layered double hydroxide nanosheets boost electrocatalytic reduction of nitrate to ammonia

Fasheng Chen [a,c], Xin-yu Zhong [d], Junjie Ding [e], Xi Chen [a], Xuemei Liao [a,c], Zhenju Jiang [a,c], Yan Xiong [b,*], Zhong Jin [b,*], Minghang Jiang [a,b,*]

[a] Department of Chemistry, School of Science, Xihua University, Chengdu, Sichuan 610039, China
[b] State Key Laboratory of Coordination Chemistry, MOE Key Laboratory of Mesoscopic Chemistry, MOE Key Laboratory of High Performance Polymer Materials and Technology, Jiangsu Key Laboratory of Advanced Organic Materials, Suzhou Key Laboratory of Green Intelligent Manufacturing of New Energy Materials and Devices, Tianchang New Materials and Energy Technology Research Center, Institute of Green Chemistry and Engineering, School of Chemistry and Chemical Engineering, Nanjing University, Nanjing, Jiangsu 210023, PR China
[c] School of Food and Biological Engineering, Xihua University, Chengdu, Sichuan 610039, China
[d] Shanghai Institute of Applied Physics, Chinese Academy of Sciences, Shanghai 201800, China
[e] College of Physics and Center of Quantum Materials and Devices, Chongqing University, Chongqing 401331, China

## GRAPHICAL ABSTRACT

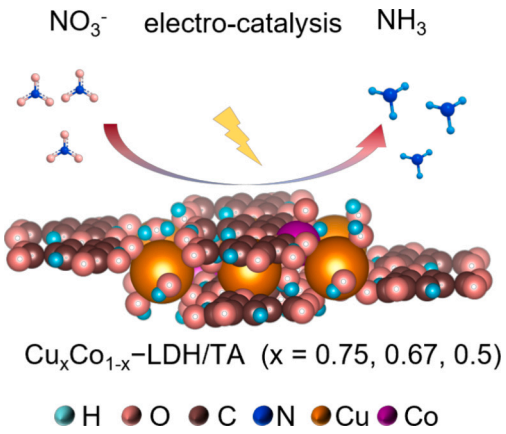


## ARTICLE INFO

*Keywords:*
Copper-cobalt layered double hydroxide
Organic molecular modification strategy
Nitrate electroreduction
ammonia synthesis

## ABSTRACT

The electrocatalytic reduction of nitrate into valuable ammonia ($NH_3$) presents an environmentally friendly and sustainable strategy for the elimination of nitrate pollution and the synthesis of ammonia. Nevertheless, the activity and selectivity for ammonia production remain unsatisfactory, particularly at low applied negative potentials. Herein, we present the synthesis of layered double hydroxide (LDH) electrocatalysts featuring adjustable Cu/Co molar ratios and organic molecule trimesic acid (TA) modification, designated as $Cu_xCo_{1-x}$-LDH/TA (x = 0.75, 0.67, or 0.5), aiming to facilitate the electrochemical nitrate reduction reaction (NITRR). Intriguingly, the microstructure, crystalline form and electrical conductivity of LDH, are substantially modified

* Corresponding authors at: Department of Chemistry, School of Science, Xihua University, Chengdu, Sichuan 610039, China.
*E-mail addresses:* xiongyan@nju.edu.cn (Y. Xiong), zhongjin@nju.edu.cn (Z. Jin), minghang@mail.xhu.edu.cn (M. Jiang).

https://doi.org/10.1016/j.jcis.2025.138664
Received 27 June 2025; Received in revised form 5 August 2025; Accepted 6 August 2025
Available online 7 August 2025
0021-9797/© 2025 Elsevier Inc. All rights are reserved, including those for text and data mining, AI training, and similar technologies.

by organic molecule TA with three carboxyl groups that play a pivotal role in bridging $[M(OH)_6]^{n-6}$ species (M = Cu or Co), thus facilitating the development of a conjugated two-dimensional layered framework. This conjugated, extended planar configuration augments the inherent conductivity, and ensures the uniform dispersion of copper and cobalt active sites on its surface, maximizing their synergistic effect during the NITRR. The resulting $Cu_{0.67}Co_{0.33}$ − LDH/TA exhibits a high $NH_3$ yield of 355.9 μmol·mg$^{-1}$·h$^{-1}$ and a Faradaic efficiency for $NH_3$ ($FE_{NH3}$) of 93.9 % for the NITRR, even at an extremely low applied negative potential of −0.6 V *versus* the reversible hydrogen electrode (*vs* RHE), which was significantly higher than that of pristine $Cu_{0.67}Co_{0.33}$ − LDH (55.0 μmol·mg$^{-1}$·h$^{-1}$ and 71.0 %, respectively). This work provides a significant reference for the utilization of organic molecules in modifying inorganic materials to boost electrocatalytic NITRR performance.

## 1. Introduction

Ammonia ($NH_3$) serves as a crucial chemical raw material in both industrial and agricultural manufacturing. Its conventional synthesis method is based on the highly energy-consuming Haber-Bosch process (H − B) [1–7]. However, the H—B process is plagued by several issues, such as high energy consumption and significant environmental pollution [8–11]. As a result, there is a pressing demand to devise a green and energy-efficient approach for synthesizing $NH_3$. The annual global combustion of fossil fuels, extensive use of nitrogen fertilizers, and significant discharge of industrial wastewater have resulted in an environment with an high nitrate content, spanning a broad concentration range from 7.4 mmol·L$^{-1}$ to 1.9 mol·L$^{-1}$ [12–16]. Moreover, an excessive accumulation of nitrates within drinking water has the potential to give rise to health-related problems in humans [17,18]. Hence, the electrochemical transformation of nitrate into $NH_3$ presents a promising strategy for nitrogen recycling and alleviating environmental pollution problems [19]. However, the electrochemical nitrate reduction reaction (NITRR) process for $NH_3$ synthesis involves intricate proton-coupled electron transfers process and faces competition from the hydrogen evolution reaction (HER). This gives rise to significant challenges, including low activity, poor selectivity, and sluggish reaction kinetics [20–23]. Consequently, it is crucial to rationally design highly efficient electrocatalysts that demonstrate excellent activity and selectivity in the electrochemical conversion of $NO_3^-$ into ammonia.

At present, Cu-based catalysts continue to stand out as preferred choices for attaining high selectivity during the electrochemical process of transforming $NO_3^-$ into $NH_3$ [13,14,24–26]. This distinct advantage arises from copper's exceptional electrical conductivity and its fully occupied 3d orbital. The unique $3d^{10}$ electronic configuration of copper enables it to function as a highly efficient catalytic active center for the reduction of $NO_3^-$ [27,28]. Meanwhile, the surfaces of Cu metal exhibit the ability to inhibit the HER [29]. However, Cu exhibits a poor ability to activate protons, thereby impeding the generation of active hydrogen (*H) on its surface. This, in turn, constrains the availability of the active hydrogen necessary for the reduction of $NO_3^-$ to $NH_3$ [30,31]. Combining copper with metals (such as cobalt) that possess the advantage of activating water molecules to generate active hydrogen for the construction of copper-based bimetallic centers may potentially address the issue of copper's insufficient hydrogen-producing capability from water activation, while preserving the advantage of copper metal centers in adsorbing nitrogen-containing species. Furthermore, an ideal copper-cobalt bimetallic center catalyst should also feature a uniform distribution of bimetallic centers, along with adjustable composition and ratios, in order to exhibit notable advantages in the electrocatalytic ammonia production process *via* NITRR.

Layered double hydroxide (LDH), belonging to the category of ionic layered materials, are distinguished by their facile adaptability in terms of chemical composition and crystalline architecture. This attribute offers significant potential for attaining a highly controllable concentration of diverse metals [32,33]. Furthermore, LDHs maintain structural stability both before and after undergoing reactions, rendering them exceptionally versatile materials with extensive applications across diverse domains such as catalysis, biology, energy storage, and photocatalysis [30]. However, the LDH catalysts' inherent limitations, including subpar electrical conductivity and insufficient electron and charge transfer capabilities, impede their potential utilization in high-performance electrochemical nitrate reduction processes [34]. Considering that a pivotal step in the formation mechanism of LDH involves the deprotonation process of Metal hydrated ion ($[M(H_2O)_6]^{n+}$) [35], and the carboxyl groups in trimesic acid (TA) readily undergo condensation reactions with $[M(OH)_6]^{n-6}$, thereby facilitating the formation of LDH. Furthermore, the molecular structure of TA demonstrates robust electron affinity and excellent structural stability, the incorporation of TA into the LDH structure can effectively ameliorate the poor conductivity and instability inherent in LDH.

Herein, we report the preparation of LDH electrocatalysts with adjustable Cu/Co molar ratios through a simple and rapid co-precipitation method at ambient temperature. It is noteworthy that the incorporation of TA organic molecules into LDH can significantly modify its microstructure, crystalline form, and electrical conductivity. Specifically, TA, endowed with three carboxyl groups, serves as a crucial linker for bridging $[M(OH)_6]^{n-6}$ species (where M denotes Cu or Co), thereby enabling the formation of a conjugated two-dimensional layered architecture. This conjugated, extended planar arrangement not only enhances the intrinsic conductivity of the material but also guarantees the homogeneous distribution of copper and cobalt active sites across its surface, optimizing their synergistic interaction during the NITRR. Furthermore, the integration of TA gives rise to the formation of an amorphous structural configuration of LDH, thereby facilitating the exposure of a substantially larger number of catalytic active sites. The obtained $Cu_{0.67}Co_{0.33}$ − LDH/TA catalyst demonstrated an impressive $NH_3$ yield of 355.9 μmol·mg$^{-1}$·h$^{-1}$ and a Faradaic efficiency for $NH_3$ ($FE_{NH3}$) of 93.9 % at an extremely low applied negative potential of −0.6 V *versus* the reversible hydrogen electrode (*vs* RHE). These values were markedly superior to those observed for the pristine $Cu_{0.67}Co_{0.33}$ − LDH catalyst without TA modification (55.0 μmol·mg$^{-1}$·h$^{-1}$ and 71.0 %, respectively). Furthermore, the $Cu_{0.67}Co_{0.33}$ − LDH/TA catalyst exhibited remarkable stability, retaining nearly unchanged catalytic activity following successive cycle tests and prolonged evaluations. This work provides fresh perspectives for future endeavors focused on improving the microstructure and physicochemical properties of inorganic materials *via* modifications using carboxyl group-rich organic molecules, with the aim of boosting their performance in electrochemical NITRR.

## 2. Experimental section

### 2.1. Chemicals and materials

Anhydrous copper chloride ($CuCl_2$, 98 %), cobalt chloride hexahydrate ($CoCl_2{\cdot}6H_2O$, 98 %), sodium hydroxide (NaOH, 95 %), p-aminobenzenesulfonic acid ($C_6H_7NO_3S$, 100 %), *p*-dimethylaminobenzaldehyde ($C_9H_{11}NO$, 99 %), sodium nitroprusside dihydrate ($C_5H_2FeN_6NaO_2{\cdot}2H_2O$, 99 %) and N-(1-naphthyl) ethylenediamine dihydrochloride ($C_{12}H_{14}N_2{\cdot}2HCl$, 98 %) were purchased from Macklin. Trimesic acid ($C_9H_6O_6$, 99 %) and $K^{15}NO_3$ (99 %) were obtained from Aladdin. $KNO_3$ (99 %), anhydrous ethanol ($C_2H_5OH$,

99.7 %), concentrated hydrochloric acid (HCl, 99 %), and sodium sulfate ($Na_2SO_4$, 99.5 %) were sourced from Kelong. All chemicals were utilized in their as-received state, without any additional purification steps. The water used as a reagent in all experimental procedures was deionized water.

### 2.2. Synthesis of $Cu_xCo_{1-x}$ − LDH/TA (x = 0.5, 0.67, 0.75)

The $Cu_xCo_{1-x}$ − LDH/TA (where x = 0.5, 0.67, 0.75) samples were synthesized using a co-precipitation method at room temperature. Specifically, for the synthesis of $Cu_{0.67}Co_{0.33}$ − LDH/TA, 0.67 mmol of $CuCl_2$ and 0.33 mmol $CoCl_2{\cdot}6H_2O$ were suspended in 20 mL of deionized $H_2O$ to form a uniform metal salt solution. 300 mg of trimesic acid (TA, 2.5 mmol) was dissolved in 10 mL of anhydrous ethanol to obtain TA-ethanol solution. Afterwards, the TA-ethanol solution was gradually added drop by drop to the metal salt solution while stirring continuously. Subsequently, the pH of the resulting mixture was adjusted to 7 by using a 1 M NaOH solution. Following filtration, thoroughly rinse the precipitate obtained with deionized water, and subsequently dry it at a temperature of 60 °C. Similarly, the synthesis processes for other $Cu_xCo_{1-x}$ − LDH/TA samples with different Cu/Co molar ratios ($Cu_{0.75}Co_{0.25}$ − LDH/TA and $Cu_{0.5}Co_{0.5}$ − LDH/TA) were the same as that of $Cu_{0.67}Co_{0.33}$ − LDH/TA by adjusting the amounts of added metal precursors solution, and the total molar amount of metal salt was 1 mmol. In the case of two control samples, CuO/TA and Co $(HCOO)_2(H_2O)_2$/TA were prepared by the same method without the addition of $CoCl_2{\cdot}6H_2O$ and $CuCl_2$, respectively, and the molar amount of metal salt was 1 mmol. Moreover, $Cu_{0.67}Co_{0.33}$ − LDH sample was synthesized by the same method as $Cu_{0.67}Co_{0.33}$ − LDH/TA but without the addition of TA.

### 2.3. Material characterizations

The surface morphology and structure of the material were investigated by scanning electron microscopy (SEM, YB-200E) and transmission electron microscopy (TEM, JEM-2100F). Elemental mapping images tests were carried out on a Talos F200i instrument. Powder X-ray diffraction (XRD) analysis was carried out by a Bruker D-8 Advance diffractometer with a Cu *Kα* X-ray source from 10 and 60° with a scanning rate of 2° $min^{-1}$. The surface element compositions and detailed valence states of all catalysts were probed by X-ray photoelectron spectroscopy (XPS) *via* a PHI-5000 Versa Probe instrument. The samples underwent analysis *via* Fourier transform infrared spectroscopy (FTIR, Nicolet IS10). The UV–Vis absorbance spectra were measured on a UV-2700 instrument. Nitrogen adsorption and desorption isotherms were determined at 77 K utilizing a Micromeritics ASAP 2020 M instrument. The surface area was computed from the adsorption data employing the Brunauer-Emmett-Teller (BET) method.

### 2.4. Electrochemical measurements

Electrochemical assessments were conducted utilizing a Chenhua CHI-760E electrochemical workstation within an H-type electrolytic cell setup. The working electrode consisted of a piece of carbon paper (CP, measuring 1 × 1.5 $cm^2$) coated with the freshly prepared electrocatalyst (with an areal loading of 0.2 mg·$cm^{-2}$), while a Pt disk electrode (1 × 1 $cm^2$) and a standard Ag/AgCl electrode served as the counter and reference electrodes, respectively. Prior to conducting the electrochemical tests, the Nafion-117 proton exchange membrane underwent a sequential treatment process. This involved immersing the membrane in an aqueous solution of 5 % $H_2O_2$ and subsequently in a 0.5 M $H_2SO_4$ solution, both at a temperature of 80 °C for a duration of 1 h each. Following these treatments, the membrane was thoroughly rinsed with deionized water to ensure complete removal of any residual chemicals. In this study, all potential values were adjusted to correspond with the reversible hydrogen electrode (RHE) scale, employing the specified equation for calibration: E (*vs.* RHE) = E (*vs.* Ag/AgCl) + 0.1989 + 0.059 × pH. All electrochemical measurements in this study were performed at room temperature.

### 2.5. Calculations of the $NH_3$ yield rates and faradaic efficiencies

The $NH_3$ yield rate ($Y_{NH3}$) can be calculated as: $Y_{NH3}$ (μmol·$h^{-1}$·$mg^{-1}$) = ($C_{NH3}$ × V)/(t × $m_{cat.}$), where $C_{NH3}$ (μmol·$L^{-1}$) is the measured $NH_3$ concentration, V (L) is the volume of the electrolyte, t (h) is the reaction time, and m (mg) is the catalyst loading mass on the CP. The Faradaic efficiency (FE) can be determined through the following formula: FE = (n × F × $C_{NH3}$ × V) / (17 × Q). Here, n represents the quantity of electrons transferred, F denotes the Faraday constant (valued at 96485C·$mol^{-1}$), V indicates the volume of the electrolyte, and Q is the total quantity of electricity applied.

## 3. Results and discussion

### 3.1. Preparation and characterizations of electrocatalysts

As depicted in Fig. 1a, the formation mechanism of metal hydroxides can be described as follows: Firstly, metal ions combine with water molecules to form metal hydrated ions ($[M(H_2O)_6]^{n+}$). Subsequently, by increasing the pH of the solution, the protons in $[M(H_2O)_6]^{n+}$ combine with $OH^-$ in the solution to form $H_2O$ molecules, a process known as deprotonation, resulting in the formation of LDH [35]. Based on the formation mechanism of LDH, the incorporation of TA can facilitate the formation of the LDH structure. Specifically, the condensation reaction takes place between $[M(OH)_6]^{n-6}$ and the carboxyl groups of TA, resulting in the formation of LDH. Moreover, considering that the molecular structure of TA exhibits strong electron affinity and good structural stability, the introduction of TA into the LDH structure can effectively improve the conductivity and instability of LDH.

As shown in Fig. 1b, the $Cu_xCo_{1-x}$ − LDH/TA (x = 0.75, 0.67, or 0.5) samples, featuring varying Cu/Co molar ratios, were synthesized using a straightforward and swift co-precipitation method at room temperature. The surface morphology of the samples was investigated utilizing field-emission scanning electron microscopy (SEM). It is observed that the obtained $Cu_{0.67}Co_{0.33}$-LDH/TA exhibits a smooth-surfaced nanosheet structure (Fig. 1c). Elemental distribution mappings for $Cu_{0.67}Co_{0.33}$-LDH/TA composite (Fig. 1d-1h) reveal homogeneous distribution of both copper and cobalt species throughout the material matrix. The homogeneous dispersion of Cu and Co facilitates synergistic interaction between the two metals, promoting efficient electrochemical NITRR. Moreover, the homogeneous distribution of carbon elements within the $Cu_{0.67}Co_{0.33}$-LDH/TA sample is distinctly observable (Fig. 1e), signifying successful uniform incorporation of TA molecules into the catalyst. Field-emission transmission electron microscopy (TEM) was utilized for detailed characterization of the $Cu_{0.67}Co_{0.33}$-LDH/TA microstructure. Fig. 1i presents TEM image of the $Cu_{0.67}Co_{0.33}$-LDH/TA sample, suggesting that the $Cu_{0.67}Co_{0.33}$-LDH/TA exhibits an amorphous nature (Fig. 1j). Moreover, $Cu_xCo_{1-x}$-LDH/TA (x = 0.75 and 0.5) samples with other Cu/Co molar ratios also exhibit similar lamellar structures (Fig. S1). However, when the metal precursor consists of only a single metal, the resulting sample morphology is entirely different from that of the $Cu_xCo_{1-x}$-LDH/TA samples (x = 0.75, 0.67, or 0.5). Specifically, when only Cu salt is added as the metal precursor, the sample exhibits a porous bulk structure (Fig. S2a and S2c). In contrast, when Co salt is used as the metal precursor, the sample presents a three-dimensional structure composed of ultrathin nanosheets (Fig. S2b and S2d). The morphologies of the $Cu_xCo_{1-x}$-LDH/TA samples (x = 0.75, 0.67, or 0.5) are markedly distinct from those of materials formed with a single metal addition (Cu or Co), reflecting significant differences in their composition and microstructure. Notably, we also investigated the influence of not adding TA on the microstructure and morphology of the formed materials. Specifically, The $Cu_{0.67}Co_{0.33}$ − LDH sample was prepared

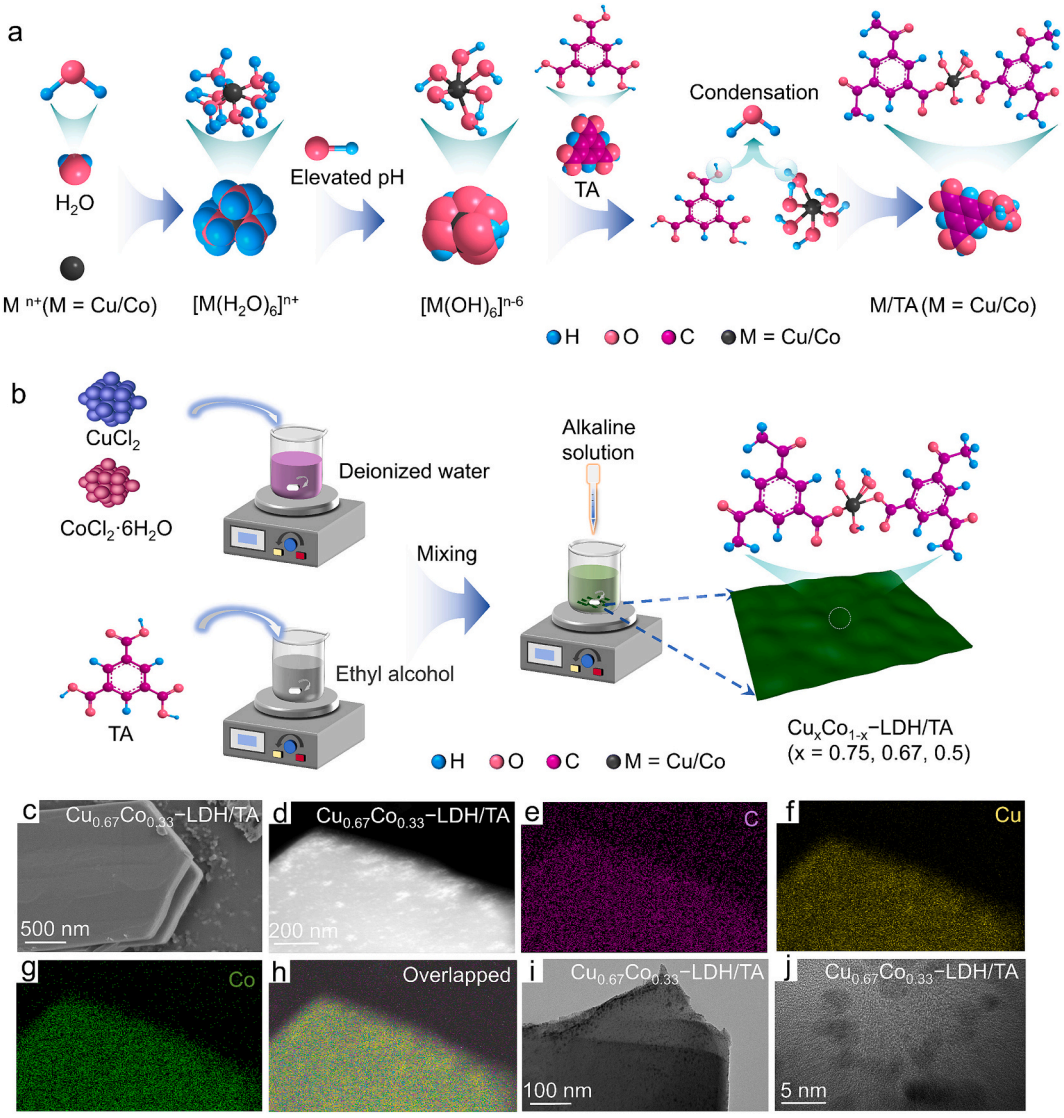


**Fig. 1.** Schematic diagram of the samples synthesis routes, morphological and structural analysis of samples. (a) A mechanism diagram of TA-modified LDH. (b) illustrates the formation process of $Cu_xCo_{1-x}$ − LDH/TA (x = 0.75, 0.67, or 0.5). (c) SEM, (d-h) elemental mapping analysis spectra, (i) TEM, and (j) HRTEM images of $Cu_{0.67}Co_{0.33}$ − LDH/TA.

using an identical synthesis approach to that of $Cu_{0.67}Co_{0.33}$ − LDH/TA, with the exception that TA was not incorporated during the process. As shown in Fig. S3, it can be clearly observed that the microstructure of the $Cu_{0.67}Co_{0.33}$-LDH sample is entirely different from that of the $Cu_{0.67}Co_{0.33}$-LDH/TA, with the material consisting of numerous fragmented small nanosheets. This could be attributed to the condensation reaction readily occurring between the carboxyl groups in TA and $[M(OH)_6]^{n-6}$, where TA acts as an intermediary link in the material structure, facilitating the formation of larger sheet-like structures. This is consistent with the TA-promoting LDH formation mechanism we described in Fig. 1a.

The crystallographic composition of the catalysts was analyzed through X-ray diffraction (XRD). As depicted in Fig. 2a, the XRD patterns of $Cu_{0.67}Co_{0.33}$-LDH/TA exhibit an amorphous nature, which is consistent with the results obtained from HRTEM analysis (Fig. 1j). However, the XRD diffraction peaks of $Cu_{0.67}Co_{0.33}$ − LDH match those of $Cu(OH)_2$ (PDF#99–000-3468) and $Co_2(OH)_3Cl$ (PDF#97–002-4685), which is obviously different with the XRD analysis outcomes of $Cu_{0.67}Co_{0.33}$ − LDH/TA. This phenomenon indicates that the incorporation of TA serves as the pivotal factor contributing to the formation of an amorphous structure. Moreover, as shown in Fig. S4a, when Cu salt is used as the metal precursor, the primary component of the sample is CuO with low crystallinity, thus the sample is named CuO/TA. Moreover, when Co salt is utilized as the metal precursor, the main constituent of the sample is $Co(HCOO)_2(H_2O)_2$ with low crystallinity, hence the sample is designated as $Co(HCOO)_2(H_2O)_2$/TA. The aforementioned phenomenon indicates that $Cu_{0.67}Co_{0.33}$-LDH/TA possesses a new composition and structure rather than a mere mixture of CuO/TA and $Co(HCOO)_2(H_2O)_2$/TA. Fig. 2b and Fig. S4b showcases the Fourier Transform Infrared Spectroscopy (FTIR) spectra for $Cu_{0.67}Co_{0.33}$ − LDH/TA, CuO/TA, and $Co(HCOO)_2(H_2O)_2$/TA. The characteristic peaks of LDH emerge at 619.5 and 774.8 $cm^{-1}$, which are ascribed to the stretching vibrations associated with M-OH bonds. (M = Cu/Co) [36]. The bending vibrations of H-O-H within the metal hydroxide layers fall within the range of 1597.7 to 1637.3 $cm^{-1}$ [37–39]. In contrast, the peaks situated at 1439.6 $cm^{-1}$ correspond to the asymmetric vibrational peak of C—O in TA [40–42]. The peaks at 524.9 and 725.1 $cm^{-1}$ are indicative of the out-of-plane bending vibration peak characteristic of the phenyl group emerges [40]. However, the FTIR spectrum of $Cu_{0.67}Co_{0.33}$ − LDH displays only the signal peaks corresponding to M-OH and H-O-H bonds, with no observable peaks indicating the presence of TA's C—O and benzene ring C═C bonds. These analysis results indicate that TA has

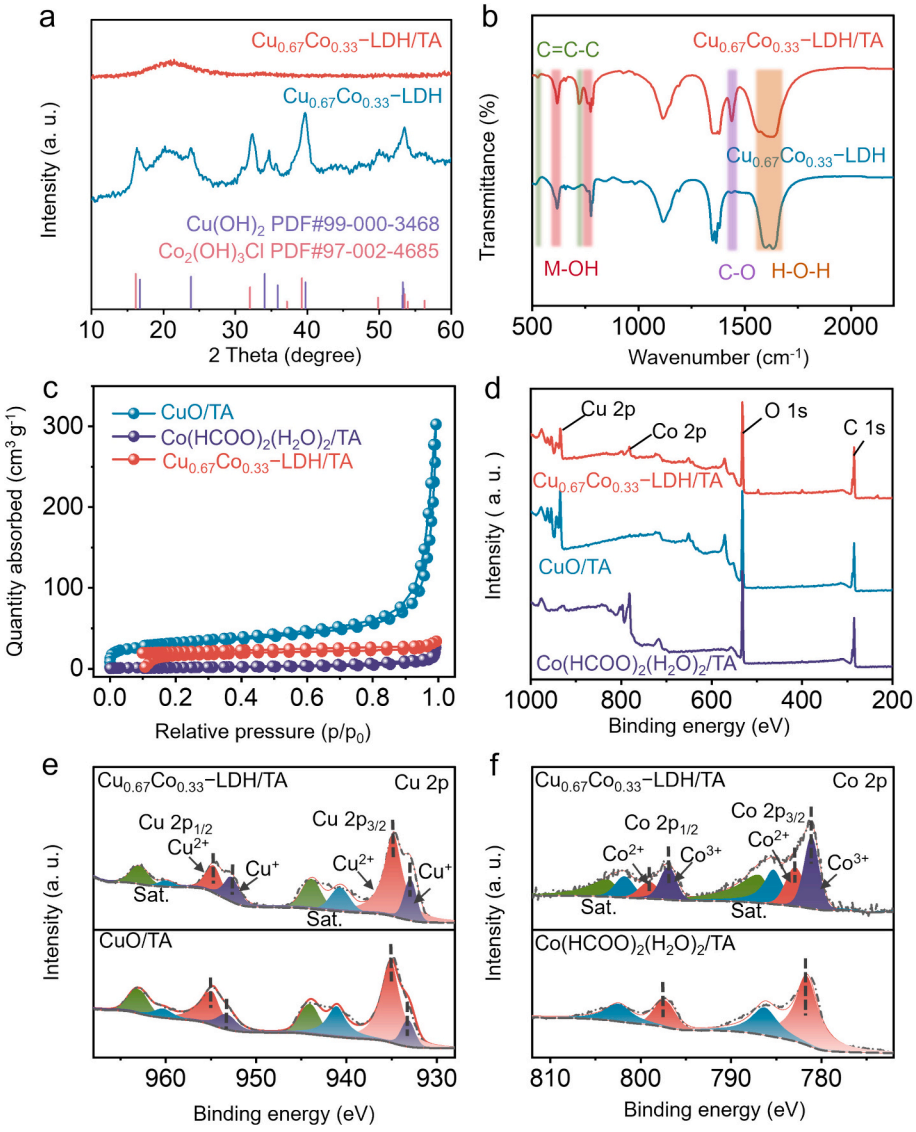


**Fig. 2.** Spectroscopic analyses of samples. (a) XRD patterns, and (b) FTIR spectra of $Cu_{0.67}Co_{0.33}$ − LDH/TA and $Cu_{0.67}Co_{0.33}$ − LDH samples. (c) nitrogen adsorption isotherms, and (d) XPS surveys of $Cu_{0.67}Co_{0.33}$ − LDH/TA, CuO/TA, $Co(HCOO)_2(H_2O)_2$/TA samples. (e) High-resolution XPS spectra at the Cu 2p of $Cu_{0.67}Co_{0.33}$ − LDH/TA and CuO/TA. (f) High-resolution XPS spectra at the Co 2p regions of $Cu_{0.67}Co_{0.33}$ − LDH/TA and $Co(HCOO)_2(H_2O)_2$/TA samples.

been successfully incorporated into the LDH structure. Moreover, the introduction of TA has significantly altered the coordination environment surrounding the metal centers within LDH, as well as its crystalline form and microscopic structure. Fig. 2c exhibits the isotherms for nitrogen adsorption and desorption in $Cu_{0.67}Co_{0.33}$ − LDH/TA, CuO/TA, and $Co(HCOO)_2(H_2O)_2$/TA. The specific surface area follows the order: CuO/TA (108 $m^2 \cdot g^{-1}$) > $Cu_{0.67}Co_{0.33}$ − LDH/TA (67 $m^2 \cdot g^{-1}$) > $Co(HCOO)_2(H_2O)_2$/TA (6 $m^2 \cdot g^{-1}$). Furthermore, as evidenced by the pore size distribution depicted in Fig. S5, $Cu_{0.67}Co_{0.33}$ − LDH/TA demonstrates a notably rich microporous architecture, CuO/TA encompasses both microporous and mesoporous features, while $Co(HCOO)_2(H_2O)_2$/TA exhibits almost negligible porosity. The specific surface area of $Cu_{0.67}Co_{0.33}$ − LDH/TA falls between that of CuO/TA and $Co(HCOO)_2(H_2O)_2$/TA, indicating that the incorporation of copper species is beneficial for increasing the material's specific surface area, thereby exposing more active sites during the electrocatalytic NITRR process.

The surface composition and valence states of the samples were analyzed utilizing X-ray photoelectron spectroscopy (XPS). The binding energies of all peaks observed in the XPS spectra were calibrated with reference to the C 1 s peak, which was set at 284.8 eV. The survey spectra of $Cu_{0.67}Co_{0.33}$ − LDH/TA, CuO/TA, and $Co(HCOO)_2(H_2O)_2$/TA samples are presented in Fig. 2d, the signal peaks from the Cu 2p, Co 2p, O 1 s, and C 1 s can be obviously observed for the $Cu_{0.67}Co_{0.33}$ − LDH/TA catalyst. Fig. S6 presents the high-resolution XPS spectra for the C 1 s and O 1 s regions of $Cu_{0.67}Co_{0.33}$ − LDH/TA, CuO/TA, and $Co(HCOO)_2(H_2O)_2$/TA. As shown in Fig. S6a, the high-resolution XPS spectrum of C 1 s can be decomposed into three distinct peaks situated at 284.8 eV, 286.2 eV, and 288.1 eV, which correspond to three different surface carbon species: non-oxidized carbon within the ligand (C − C), oxygen-containing carbon (C − O), and carboxyl carbon (O=C − O), respectively [43]. This observation suggests that TA has been successfully incorporated into the structural frameworks of the $Cu_{0.67}Co_{0.33}$ − LDH/TA, CuO/TA, and $Co(HCOO)_2(H_2O)_2$/TA samples, a finding that aligns with the results derived from the FTIR spectral analysis. Moreover, the high-resolution XPS spectrum of O 1 s (Fig. S6b) exhibits three distinct peaks at 530.9 eV, 531.8 eV, and 532.9 eV, which are attributable to three different surface oxygen species: metal-oxygen bonds (M − O), oxygen vacancy ($O_v$), and molecular oxygen from adsorbed $H_2O$ on the sample surface ($H_2O_{abs}$), respectively [44–47]. As illustrated in Fig. 2e, for the $Cu_{0.67}Co_{0.33}$ − LDH/TA and CuO/TA samples, the high-

resolution XPS spectrum within the Cu 2p region can be resolved into six characteristic peaks. Among these, the peaks at 934.8 eV and 954.6 eV correspond to the signal peaks of $Cu^{2+}$, while the peaks at 932.9 eV and 952.6 eV are indicative of $Cu^{+}$ states. Moreover, the peaks located at 940.7 eV, 943.8 eV, 959.9 eV, and 962.9 eV are attributed to the satellite (Sat.) peaks [48,49]. Furthermore, for the $Cu_{0.67}Co_{0.33}$ − LDH/TA and $Co(HCOO)_2(H_2O)_2$/TA samples, the peaks situated at 785.3, 786.8, 801.8, and 803.6 eV correspond to Sat. peaks. The signal peaks at 782.8 eV and 799.0 eV are attributed to $Co^{2+}$, while those at 781.0 eV and 796.8 eV are attributed to $Co^{3+}$ [46,50]. It is worth mentioning that the Cu 2p spectrum of $Cu_{0.67}Co_{0.33}$ − LDH/TA displays a shift of its peaks towards higher binding energies in comparison to that of CuO/TA. Conversely, a negative shift is observed in the Co 2p spectrum of $Cu_{0.67}Co_{0.33}$ − LDH/TA when contrasted with that of Co $(HCOO)_2(H_2O)_2$/TA. This phenomenon indicates the presence of electronic interactions between Cu and Co [51,52].

X-ray absorption spectroscopy (XAS) was employed to carry out a comprehensive analysis of the valence states, bond lengths, and coordination numbers pertaining to the Cu or Co elements within the $Cu_{0.67}Co_{0.33}$ − LDH/TA, CuO/TA, and $Co(HCOO)_2(H_2O)_2$/TA samples [53]. Based on the findings from Cu K-edge X-ray absorption near-edge spectroscopy (XANES) analysis (Fig. 3a), when compared to the absorption edges of Cu foil, $Cu_2O$, and CuO, the absorption edges of $Cu_{0.67}Co_{0.33}$ − LDH/TA and CuO/TA exhibit a shift towards higher energy ranges, closely mirroring the absorption edge of CuO. This observation implies that the Cu in these samples exists in an oxidized state.

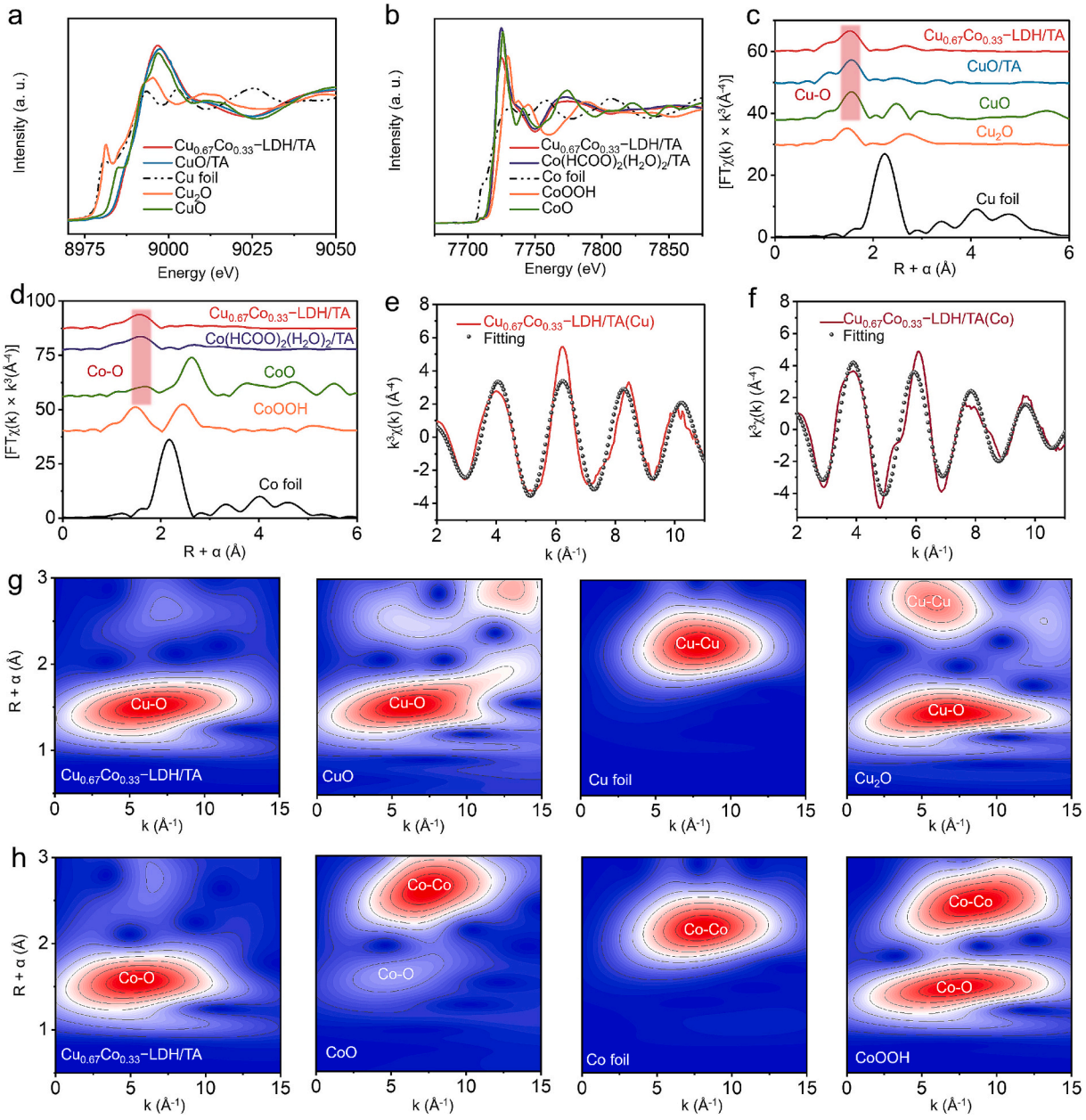


**Fig. 3.** (a) Cu K-edge XANES spectra of $Cu_{0.67}Co_{0.33}$ − LDH/TA, CuO/TA, Cu foil, $Cu_2O$, and CuO samples. (b) Co K-edge XANES spectra of $Cu_{0.67}Co_{0.33}$ − LDH/TA, $Co(HCOO)_2(H_2O)_2$/TA, Co foil, CoO, and CoOOH samples. (c) Fourier transformations of the $k^3$-weighted χ(k)-function of the EXAFS spectra at Cu K-edge of $Cu_{0.67}Co_{0.33}$ − LDH/TA, CuO/TA, Cu foil, $Cu_2O$, and CuO samples. (d) Fourier transformations of the $k^3$-weighted χ(k)-function of the EXAFS spectra at Co K-edge of $Cu_{0.67}Co_{0.33}$ − LDH/TA, $Co(HCOO)_2(H_2O)_2$/TA, Co foil, CoOOH, and CoO samples. (e) The fitting result of the EXAFS spectrum of $Cu_{0.67}Co_{0.33}$ − LDH/TA for the Cu element at k-space. (f) The fitting result of the EXAFS spectrum of $Cu_{0.67}Co_{0.33}$ − LDH/TA for the Co element at k-space. (g) WT of the Cu K-edge FT-EXAFS spectra of $Cu_{0.67}Co_{0.33}$ − LDH/TA, CuO, Cu foil, and $Cu_2O$ samples. (h) WT of the Co K-edge FT-EXAFS spectra of $Cu_{0.67}Co_{0.33}$ − LDH/TA, CoO, Co foil, and CoOOH samples.

Similarly, as illustrated in Fig. 3b, the Co K-edge XANES spectra of $Cu_{0.67}Co_{0.33}$ − LDH/TA and $Co(HCOO)_2(H_2O)_2$/TA closely correspond to the absorption edge of CoO, indicating the presence of oxidized Co [54,55]. The aforementioned analysis results are consistent with the XRD analysis results. Moreover, the coordination environments of $Cu_{0.67}Co_{0.33}$ − LDH/TA, CuO/TA, and $Co(HCOO)_2(H_2O)_2$/TA were further examined through Extended X-ray Absorption Fine Structure (EXAFS) spectra (Fig. 3c-3f and Fig. S7). Fig. 3c presents the R-space plots for $Cu_{0.67}Co_{0.33}$ − LDH/TA and CuO/TA, featuring a prominent peak at 1.55 Å, which is characteristic of Cu—O coordination. Furthermore, as outlined in Table S1, the Cu—O bond lengths in both $Cu_{0.67}Co_{0.33}$ − LDH/TA and CuO/TA measure approximately 1.96 Å, consistent with the Cu—O bond length observed in standard CuO samples. This confirms that the Cu element in $Cu_{0.67}Co_{0.33}$ − LDH/TA and CuO/TA exists in the form of Cu—O coordination. Similarly, the R-space plots of $Cu_{0.67}Co_{0.33}$ − LDH/TA and $Co(HCOO)_2(H_2O)_2$/TA exhibit a prominent peak at 1.59 Å (Fig. 3d), signifying characteristic Co—O coordination. As detailed in Table S2, the Co—O bond lengths in $Cu_{0.67}Co_{0.33}$ − LDH/TA and $Co(HCOO)_2(H_2O)_2$/TA (2.09 Å) closely match the Co—O bond length observed in standard CoO samples (2.10 Å). This confirms that the Co element in both $Cu_{0.67}Co_{0.33}$ − LDH/TA and $Co(HCOO)_2(H_2O)_2$/TA exists in the form of Co—O coordination. Furthermore, the wavelet transformation (WT) analysis of the Cu K-edge Fourier transform (FT) EXAFS for $Cu_{0.67}Co_{0.33}$ − LDH/TA (Fig. 3g) indicates that the bonding mode of Cu is Cu—O (at 6.5 $Å^{-1}$) when compared to reference standard samples. Meanwhile, the WT analysis of the Co K-edge FT EXAFS for $Cu_{0.67}Co_{0.33}$ − LDH/TA (Fig. 3h) corresponds to Co—O bending. The analysis results align exceptionally well with those obtained from EXAFS analysis. As for the CuO/TA and $Co(HCOO)_2(H_2O)_2$/TA samples, as shown in Fig. S8, the WT analysis results of the Cu or Co K-edge FT EXAFS are consistent with those obtained from the WT analysis of $Cu_{0.67}Co_{0.33}$ − LDH/TA.

### 3.2. Electrocatalytic nitrate reduction performances

We assessed the NITRR performance were carried out within an H-type cell, which was partitioned by a Nafion 117 membrane, under ambient conditions (Fig. S9). The linear sweep voltammetry (LSV) curves depicted in Fig. 4a indicate that, within the potential window spanning from −0.5 to −0.9 V *vs* RHE, the $Cu_{0.67}Co_{0.33}$ − LDH/TA sample demonstrates a notably higher current density in a 0.1 M $Na_2SO_4$ solution containing 0.01 M $NO_3^-$, as opposed to a 0.1 M $Na_2SO_4$ solution without $NO_3^-$. This observation implies the likely occurrence of the NITRR in the $Na_2SO_4$ solution when $NO_3^-$ is present. Similarly, both CuO/TA and $Co(HCOO)_2(H_2O)_2$/TA samples exhibit a markedly higher current density within the same potential window in a 0.1 M $Na_2SO_4$ solution containing 0.01 M $NO_3^-$, compared to a 0.1 M $Na_2SO_4$ solution without $NO_3^-$, suggesting that electrocatalytic NITRR may also occur (Fig. S10 and 4b). To investigate the catalytic capabilities of the $Cu_{0.67}Co_{0.33}$-LDH/TA sample, chronoamperometry tests were carried out over a 10-min duration across a range of applied potentials from −0.5 to −0.9 V *vs* RHE (Fig. 4c). Fig. 4d displays the ultraviolet-visible (UV–vis) absorption spectra of product solutions after coloured with indophenol blue indicator, with $Cu_{0.67}Co_{0.33}$-LDH/TA employed as the

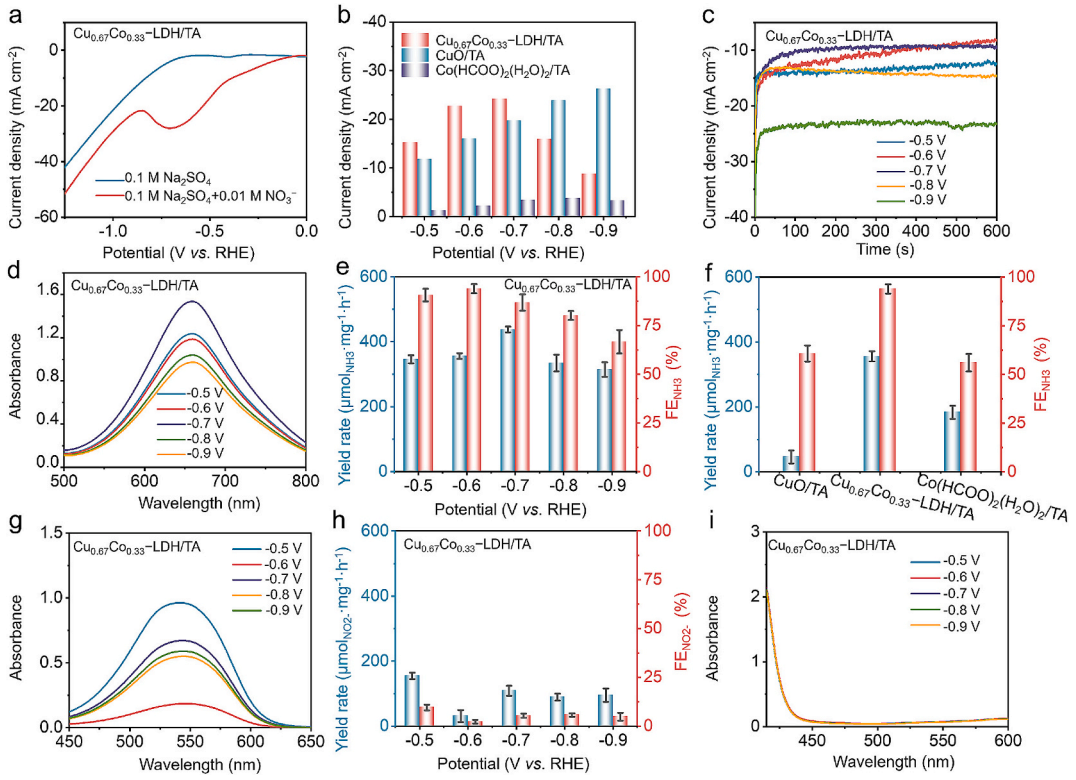


**Fig. 4.** The NITRR performance of the samples. (a) The LSV curves of $Cu_{0.67}Co_{0.33}$ − LDH/TA was tested in 0.1 M $Na_2SO_4$ solution with or without 0.01 M $NO_3^-$. (b) Comparison of geometric current densities varied with potentials for the $Cu_{0.67}Co_{0.33}$ − LDH/TA sample. (c) Time-dependent current density curves of the $Cu_{0.67}Co_{0.33}$ − LDH/TA samples under different applied potentials for the NITRR. (d) UV–vis absorption spectra of the electrolytes after the NITRR test of the $Cu_{0.67}Co_{0.33}$ − LDH/TA samples for 10 min at different potentials and coloured with indophenol indicator. (e) The $NH_3$ yield and corresponding FE values of $Cu_{0.67}Co_{0.33}$ − LDH/TA at different applied potentials for electrocatalytic NITRR (Error bars are made using the standard deviation of three experiment repeats). (f) Comparison of the $NH_3$ yield and $FE_{NH3}$ values of different catalysts at −0.6 V *vs* RHE (Error bars are made using the standard deviation of three experiment repeats). (g) UV–Vis absorption spectra of the electrolyte solution after the NITRR test of $Cu_{0.67}Co_{0.33}$ − LDH/TA at various applied potentials and then coloured by the Griess indicator. (h) The $NO_2^-$ yield and corresponding $FE_{NO2-}$ values of $Cu_{0.67}Co_{0.33}$ − LDH/TA at given potentials for the NITRR (Error bars are made using the standard deviation of three experiment repeats). (i) UV–Vis absorption spectra of the electrolyte solution after the NITRR test of $Cu_{0.67}Co_{0.33}$ − LDH/TA for 10 min within the potential range of −0.5 V to −0.9 V *vs* RHE and then coloured by the para-dimethylamino-benzaldehyde indicator.

cathodic electrocatalyst. Fig. S11a illustrates the ultraviolet-visible (UV–vis) absorption spectra of standard ammonia solutions across various concentrations, accompanied by the respective calibration curves shown in Fig. S11b. Notably, Fig. S11b reveals a strong linear correlation between the light absorbance measured at a wavelength of 665 nm and the ammonia concentration. By employing the $NH_3$ standard curve illustrated in Fig. S11b, the $NH_3$ yield and the associated $FE_{NH3}$ values for the $Cu_{0.67}Co_{0.33}$-LDH/TA catalyst were calculated at various potentials. Fig. 4e illustrates that the $Cu_{0.67}Co_{0.33}$-LDH/TA electrocatalyst achieves the highest $NH_3$ yield of 437.6 $\mu mol \cdot mg^{-1} \cdot h^{-1}$ at −0.7 V *vs* RHE and attains the maximum $FE_{NH3}$ value of 93.9 % at −0.6 V *vs* RHE. Furthermore, considering the uncertainty of nitrate wastewater concentrations in real-world environments, evaluating the practical applicability of catalysts is of critical importance. As illustrated in Fig. S12, $Cu_{0.67}Co_{0.33}$-LDH/TA demonstrates a remarkable $FE_{NH3}$ exceeding 85 % across a broad nitrate concentration range (0.005–0.5 M), while maintaining $FE_{NH3}$ values above 80 % under diverse high-salinity conditions spanning 0.1 to 2 M. These findings indicate that $Cu_{0.67}Co_{0.33}$-LDH/TA demonstrates robust performance in both varying nitrate concentrations and high-salt environments. Moreover, the NITRR performance of CuO/TA and $Co(HCOO)_2(H_2O)_2$/TA samples was also evaluated using the same characterization methods (Fig. S13). At an applied potential of −0.6 V *vs* RHE, the $NH_3$ yield and $FE_{NH3}$ of $Cu_{0.67}Co_{0.33}$-LDH/TA (355.9 $\mu mol \cdot mg^{-1} \cdot h^{-1}$ and 93.9 %, respectively) are notably higher compared to those of CuO/TA (183.5 $\mu mol \cdot mg^{-1} \cdot h^{-1}$ and 56.4 %, respectively) and $Co(HCOO)_2(H_2O)_2$/TA (46.1 $\mu mol \cdot mg^{-1} \cdot h^{-1}$ and 61.1 %, respectively) (Fig. 4f).

The Cu/Co molar ratios in $Cu_xCo_{1-x}$ − LDH/TA (where x = 0.75, 0.67, or 0.5) samples exert a notable influence on the $NH_3$ yield and $FE_{NH3}$ during the NITRR (Fig. S14). Specifically, compared to CuO/TA and $Co(HCOO)_2(H_2O)_2$/TA, the coexistence of Cu and Co in $Cu_xCo_{1-x}$ − LDH/TA (where x = 0.75, 0.67, or 0.5) can effectively enhance the performance of the NITRR (Fig. 4f and Fig. S15). However, when the molar ratio of Co increases to 50 %, the NITRR performance decreases significantly. This phenomenon may be attributed to the differing roles played by Cu and Co metal centers in the NITRR process. In the $Cu_xCo_{1-x}$ − LDH/TA (where x = 0.75, 0.67, or 0.5) catalyst, the Cu metal center serves as the primary active site for the NITRR, while the Co metal center facilitates the activation of $H_2O$ molecules to generate active hydrogen, which is essential for $NH_3$ production in the NITRR process. The concentration of active hydrogen on the catalyst surface significantly influences $NH_3$ generation in NITRR. During the $NH_3$ production process of NITRR, when the concentration of active hydrogen is within the dynamic equilibrium range between its generation and consumption, it promotes the selective hydrogenation of nitrogen-containing species to form $NH_3$ as the product. However, when the Co content in the catalyst is relatively high, an excessive concentration of adsorbed active hydrogen on the catalyst surface leads to an intense HER side reaction, thereby reducing the $NH_3$ production performance. Additionally, we examined the influence of TA introduction on NITRR performance. As shown in Fig. S16, the NITRR performance of $Cu_{0.67}Co_{0.33}$ − LDH was evaluated. Fig. 4e and Fig. S16c reveal that, at a potential of −0.6 V *vs* RHE, $Cu_{0.67}Co_{0.33}$ − LDH/TA exhibited a substantial 6.3-fold enhancement in $NH_3$ yield and a 1.3-fold increase in $FE_{NH3}$ compared to $Cu_{0.67}Co_{0.33}$ − LDH.

To elucidate the origin of the observed performance enhancement, electrochemical active surface area (ECSA) and electrochemical impedance spectroscopy (EIS) analyses were performed on $Cu_{0.67}Co_{0.33}$ − LDH/TA and $Cu_{0.67}Co_{0.33}$ − LDH. As illustrated in Fig. S17, cyclic voltammetry (CV) tests were carried out at different scan rates within the non-Faradaic potential range to assess and compare the electrochemical characteristics of the two materials. Double-layer capacitance ($C_{dl}$) values were determined by plotting anodic charging currents *versus* scan rates under open-circuit conditions, yielding 0.161 0.161 μF $cm^{-2}$ for $Cu_{0.67}Co_{0.33}$ − LDH/TA and 0.102 μF $cm^{-2}$ for $Cu_{0.67}Co_{0.33}$ − LDH. Given the direct proportionality between ECSA and $C_{dl}$, these findings demonstrate that $Cu_{0.67}Co_{0.33}$ − LDH/TA possesses a significantly larger electrochemically active surface area than that of $Cu_{0.67}Co_{0.33}$ − LDH sample. Moreover, as shown in Fig. S18, The Nyquist plots were analyzed and fitted utilizing an equivalent circuit model (inset of Fig. S18). Notably, the charge transfer resistance ($R_{ct}$) value for $Cu_{0.67}Co_{0.33}$ − LDH/TA was determined to be 23.47 Ω, significantly lower than the 75.33 Ω observed for $Cu_{0.67}Co_{0.33}$ − LDH, indicating faster kinetic processes in the former. Additionally, we investigated the effects of varying TA loading on the catalyst's crystalline structure and its NITRR performance. As illustrated in Fig. S19a, the incorporation of TA induced the formation of an amorphous structure within the catalyst. Concurrently, as TA was added, the catalyst's active site count increased, leading to a progressive enhancement in both the ammonia yield and $FE_{NH3}$, as depicted in Fig. S19b. This observation indicates that the introduction of TA significantly enhances the ammonia production performance during NITRR. This improvement is primarily attributed to the coordination formation between TA and the metal centers within LDH, which acts as a bridge between different metal centers. Consequently, these changes modify the composition and structure of the LDH. This modification regulates its the microstructure and physicochemical properties. Meanwhile, it promotes the formation of an amorphous structure within the LDH. Such an amorphous structure facilitates the generation of "dangling bonds" and provides a greater number of catalytic sites during the electrochemical NITRR process. Furthermore, as shown in Table S3, the $Cu_{0.67}Co_{0.33}$ − LDH/TA catalyst demonstrates superior catalytic performance compared to recently reported NITRR electrocatalysts for $NH_3$ production.

Furthermore, the concentration of possible by-products, like $NO_2^-$, present in the electrolyte solution were measured (Fig. S20 and 4g). Within the potential window ranging from −0.5 V to −0.9 V *vs* RHE, the $FE_{NO2}^-$ for $Cu_{0.67}Co_{0.33}$-LDH/TA remained below 10 %. Moreover, at −0.6 V *vs* RHE, $Cu_{0.67}Co_{0.33}$-LDH/TA exhibited the lowest $NO_2^-$ yield of 26.6 $\mu mol \cdot mg^{-1} \cdot h^{-1}$ and an $FE_{NO2}^-$ of 1.8 % (Fig. 4h). However, as shown in Fig. S21a and S21b, within the potential window spanning from −0.5 V to −0.9 V *vs* RHE, the electrocatalytic NITRR process over CuO/TA exhibits a significantly higher $FE_{NO2}^-$ compared to that over $Cu_{0.67}Co_{0.33}$-LDH/TA. For $Co(HCOO)_2(H_2O)_2$/TA, when a negative voltage lower than −0.7 V *vs* RHE is applied, virtually no $NO_2^-$ production is detected in the product solution (Fig. S21c and S21d). Based on the aforementioned analytical results, we deduce that the presence Co species facilitate the rapid transformation of $NO_2^-$ when a relatively small negative voltage is applied, thereby promoting the conversion of nitrate ions into ammonia as the final product. Furthermore, the Watt and Chrisp method was utilized to detect the potential by-product $N_2H_4$. Fig. S22 and 4i distinctly illustrate that no $N_2H_4$ was detected throughout the electrochemical NITRR.

To exclude potential $NH_3$ contamination from external environmental sources, a series of control experiments were conducted. Initially, as shown in Fig. 5a, a control experiment was conducted using $Cu_{0.67}Co_{0.33}$ − LDH/TA in 0.1 M $Na_2SO_4$ at −0.6 V *vs* RHE, revealing no detectable $NH_3$ production. Similarly, an electrolysis test was performed on the $Cu_{0.67}Co_{0.33}$ − LDH/TA sample in a 0.1 M $Na_2SO_4$ solution containing 0.01 M $NO_3^-$ at the open-circuit potential (OCP), and no $NH_3$ was detected. Furthermore, chronoamperometry tests using bare carbon paper (CP) as the working electrode in 0.1 M $Na_2SO_4$ + 0.01 M $NO_3^-$ at −0.6 V *vs* RHE showed no $NH_3$ was generated. More importantly, Fig. 5b illustrates the $^1H$ NMR spectra of the electrolyte following the electrocatalytic reduction of $^{15}NO_3^-$, which exhibit the characteristic double peaks indicative of $^{15}NH_4^+$. Conversely, when $^{14}NO_3^-$ was employed as the nitrogen source, only $^{14}NH_4^+$, accompanied by a triplet coupling peak, was detected. The aforementioned results demonstrate that the $NH_3$ product originates from the electroreduction of $NO_3^-$ on the $Cu_{0.67}Co_{0.33}$ − LDH/TA catalyst, rather than ammonia contamination in the external environment.

Stability serves as a paramount criterion for evaluating the performance of electrocatalysts. Consequently, the cyclic stability and long-

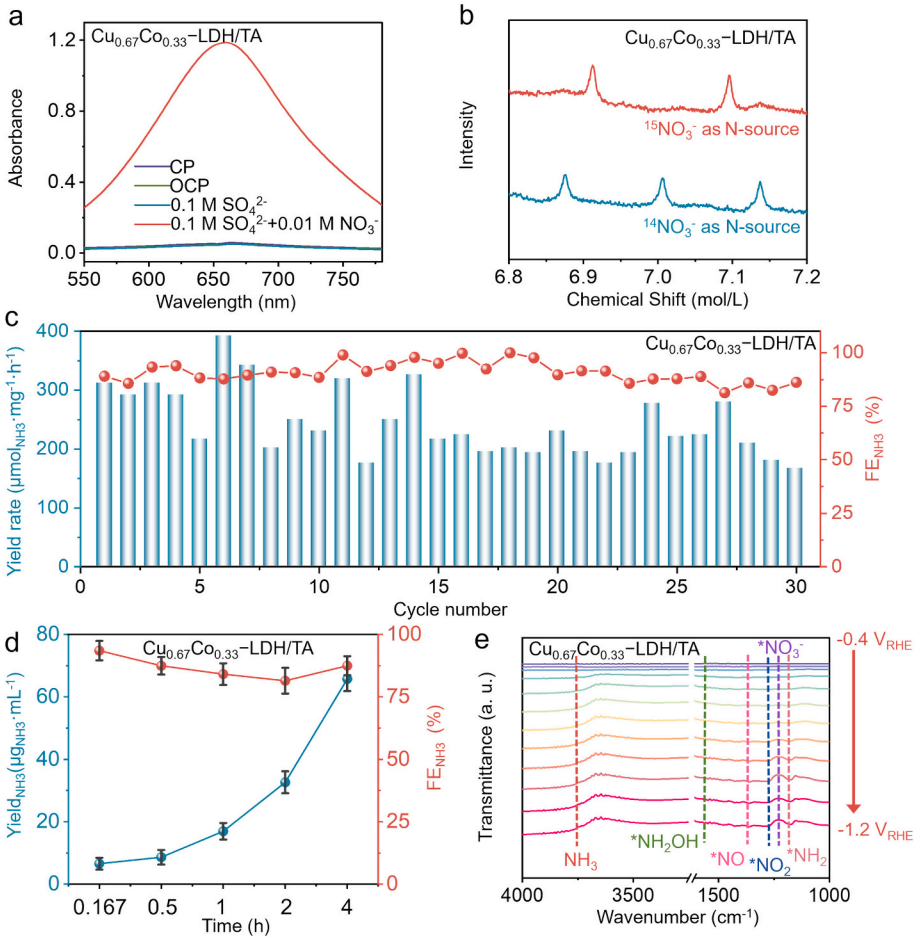


**Fig. 5.** (a) UV–vis absorption spectra after 10 min of electrolysis at −0.6 V *vs* RHE for $Cu_{0.67}Co_{0.33}$ − LDH/TA sample under various conditions and coloured with indophenol indicator. (b) $^1H$ NMR spectra of the electrolyte after the NITRR test of $Cu_{0.67}Co_{0.33}$ − LDH/TA using $^{15}NO_3^-$ and $^{14}NO_3^-$ as the N-sources, respectively. (c) Cycling stability of $Cu_{0.67}Co_{0.33}$ − LDH/TA for the NITRR during 30 cycles at −0.6 V *vs* RHE. (d) Time-dependent $NH_3$ concentration and corresponding $FE_{NH3}$ after different reaction durations of $Cu_{0.67}Co_{0.33}$ − LDH/TA at a potential of −0.6 V *vs* RHE (Error bars are made using the standard deviation of three experiment repeats). (e) *In* − *situ* infrared spectra of $Cu_{0.67}Co_{0.33}$ − LDH/TA sample at different negative applied potentials in the 0.1 M $Na_2SO_4$ electrolytes containing 0.01 M $NO_3^-$.

term durability of $Cu_{0.67}Co_{0.33}$ − LDH/TA were also assessed. As depicted in Fig. 5c, the outcomes of 30 successive cyclic tests conducted on $Cu_{0.67}Co_{0.33}$ − LDH/TA reveal no significant alterations in $FE_{NH3}$, suggesting that the NITRR performance remains well-preserved. In addition, Fig. 5d shows that as electrolysis time increases, the ammonia concentration rises proportionally. However, $FE_{NH3}$ decreases with time due to the progressive decrease in $NO_3^-$ concentration in the electrolyte. This suggests that $Cu_{0.67}Co_{0.33}$ − LDH/TA can continuously produce ammonia by consuming $NO_3^-$ in the electrolyte. Additionally, the temporal evolution of nitrate concentration in the electrolyte was systematically monitored throughout extended durability testing, with the corresponding removal efficiency calculated based on quantitative analysis (Fig. S23 and S24). As the testing duration progressed, a consistent decline in nitrate concentration was observed, paralleled by a steady enhancement in removal efficiency. Notably, electrocatalysis with $Cu_{0.67}Co_{0.33}$ − LDH/TA in 0.1 M $Na_2SO_4$ containing 0.01 M $NO_3^-$ at −0.6 V *vs* RHE for 4 h yielded a residual $NO_3^-$ concentration of 31.2 $\mu g \cdot mL^{-1}$, corresponding to a remarkable removal efficiency of 94.1 %. These findings demonstrate that the catalyst sustains superior stability even when operating under challenging low-nitrate-concentration conditions (0.01 M).

To acquire a more profound comprehension of the NITRR mechanism on $Cu_{0.67}Co_{0.33}$ − LDH/TA, *in-situ* FTIR spectroscopy analysis was utilized to investigate the potential-dependent interfacial reactions occurring on the sample's surface during electrochemical NITRR. Fig. 5e showcases across this potential range, the intensities of the peaks vary in response to the applied potential. In particular, the peak observed at 1269 $cm^{-1}$ signifies the N − O antisymmetric stretching vibration of $*NO_2$, which serves as a crucial intermediate in the rate-determining step of the reaction. Additionally, the peaks situated at 1184, 1585, and 1361 $cm^{-1}$ are assigned to the adsorbed intermediates $*NH_2$, $*NH_2OH$, and *NO, respectively. Lastly, the peak at 3761 $cm^{-1}$ signifies the formation of the product $NH_3$ [56–59]. As the reaction potential shifts towards more negative values, the intensity of the $*NH_2$ characteristic peak progressively increases. Based on the above analysis, we propose that the reaction proceeds *via* the following pathway: $*NO_3 \rightarrow *NO_2 \rightarrow *NO \rightarrow * NH_2OH \rightarrow * NH_2 \rightarrow *NH_3$. Specifically, the initial stage entails the conversion of $*NO_3$ into $*NO_2$, followed by the further reduction of $*NO_2$ to *NO. Serving as a pivotal intermediate, *NO undergoes protonation to yield $*NH_2OH$. Subsequently, $*NH_2OH$ undergoes hydrogenation, resulting in the formation of $*NH_2$, which is then electrochemically reduced to $NH_3$.

## 4. Conclusions

In summary, we demonstrate the $Cu_xCo_{1-x}$ − LDH/TA samples (where x = 0.75, 0.67, or 0.5), featuring varying Cu/Co molar ratios, were prepared using a straightforward and swift co-precipitation technique at room temperature. Unlike previous studies that utilized layered double hydroxides (LDHs) as electrocatalysts for the nitrate reduction

reaction (NITRR) [30,34], this work focuses on enhancing NITRR performance by modifying the physicochemical properties (such as microstructure, crystallinity, and electrical conductivity) of LDH through the incorporation of the organic molecule trimesic acid (TA). Specifically, the TA with three carboxyl groups is advantageous for bridging $[M(OH)_6]^{n-6}$ (M = Cu or Co) species centered around copper or cobalt metals, thereby enabling the formation of conjugated two-dimensional layered structure. This conjugated, extended planar architecture not only enhances the intrinsic conductivity of the material but also facilitates the uniform distribution of copper and cobalt active sites across its surface, thereby fully leveraging their synergistic effects during the NITRR. Moreover, the incorporation of TA induces the formation of an amorphous structural framework within the LDH, consequently promoting the exposure of a significantly greater quantity of catalytic active sites. Benefitting from the compositional and structural modifications of LDH by TA, the resulting $Cu_{0.67}Co_{0.33}$ − LDH/TA catalyst demonstrated a remarkable 6.3-fold enhancement in $NH_3$ yield and a 1.3-fold increase in Faradaic efficiency for $NH_3$ production ($FE_{NH3}$) compared to pristine LDH (without TA modification), even at an extremely low applied negative potential of −0.6 V *versus* the reversible hydrogen electrode (*vs* RHE). Moreover, the $FE_{NH3}$ of the $Cu_{0.67}Co_{0.33}$ − LDH/TA catalyst reached 93.9 %, surpassing those of previously reported LDH electrocatalysts, such as CuCo-LDHs (74.5 %) [30], CoAl-LDH (90.3 %) [60], and NiCo-LDH (85 %) [61]. This study offers substantial reference value for subsequent research aimed at enhancing the electrocatalytic performance of inorganic materials by modifying their microstructure and physicochemical properties through organic molecules.

## CRediT authorship contribution statement

**Fasheng Chen:** Writing – review & editing, Writing – original draft, Visualization, Software, Formal analysis, Data curation. **Xin-yu Zhong:** Resources. **Junjie Ding:** Resources. **Xi Chen:** Software. **Xuemei Liao:** Resources. **Zhenju Jiang:** Resources. **Yan Xiong:** Resources. **Zhong Jin:** Supervision, Resources, Funding acquisition. **Minghang Jiang:** Writing – review & editing, Supervision, Resources, Funding acquisition.

## Declaration of competing interest

The authors declare that they have no known competing financial interests or personal relationships that could have appeared to influence the work reported in this paper.

## Acknowledgements

The authors appreciate the financial support from the National Natural Science Foundation of China (22479074 and 22475096), the Natural Science Foundation of Sichuan Province (2023NSFSC1074), the Talent Introduction Plan of Xihua University (Z222051), the General Project of the Joint Fund of Equipment Preresearch and the Ministry of Education (8091B02052407), the Natural Science Foundation of Jiangsu Province (BK20240400 and BK20241236), the Science and Technology Major Project of Jiangsu Province (BG2024013), the Scientific and Technological Achievements Transformation Special Fund of Jiangsu Province (BA2023037), the Academic Degree and Postgraduate Education Reform Project of Jiangsu Province (JGKT24_C001), the Key Core Technology Open Competition Project of Suzhou City (SYG2024122), the open research fund of Suzhou Laboratory (SZLAB-1308-2024-TS005), the Gusu Leading Talent Program of Scientific and Technological Innovation and Entrepreneurship of Wujiang District in Suzhou City (ZXL2021273), and the Chenzhou National Sustainable Development Agenda Innovation Demonstration Zone Provincial Special Project (2023sfq11).

## Appendix A. Supplementary data

Supplementary data to this article can be found online at https://doi.org/10.1016/j.jcis.2025.138664.

## Data availability

Data will be made available on request.

## References

[1] M. Zhang, Z. Zhang, S. Zhang, Z. Zhuang, K. Song, K. Paramaiah, M. Yi, H. Huang, D. Wang, Efficient electrochemical nitrate reduction to ammonia driven by a few nanometer-confined built-in electric field, ACS Catal. 14 (2024) 10437–10446.
[2] H. Lin, J. Wei, Y. Guo, Y. Li, X. Lu, C. Zhou, S. Liu, Y.y. Li, $Bi_1$-$CuCo_2O_4$ hollow carbon nanofibers boosts $NH_3$ production from electrocatalytic nitrate reduction, Adv. Funct. Mater. 34 (2024) 2409696.
[3] Y. Li, H.S. Pillai, T. Wang, S. Hwang, Y. Zhao, Z. Qiao, Q. Mu, S. Karakalos, M. Chen, J. Yang, D. Su, H. Xin, Y. Yan, G. Wu, High-performance ammonia oxidation catalysts for anion-exchange membrane direct ammonia fuel cells, Energy Environ. Sci. 14 (2021) 1449–1460.
[4] L. Bai, F. Franco, J. Timoshenko, C. Rettenmaier, F. Scholten, H.S. Jeon, A. Yoon, M. Rüscher, A. Herzog, F.T. Haase, S. Kühl, S.W. Chee, A. Bergmann, R.C. Beatriz, Electrocatalytic nitrate and nitrite reduction toward ammonia using $Cu_2O$ nanocubes: active species and reaction mechanisms, J. Am. Chem. Soc. 146 (2024) 9665–9678.
[5] J. Zhang, T. Quast, B. Eid, Y.-T. Chen, R. Zerdoumi, S. Dieckhöfer, J.R. C. Junqueira, S. Seisel, W. Schuhmann, *In-situ* electrochemical reconstruction and modulation of adsorbed hydrogen coverage in cobalt/ruthenium-based catalyst boost electroreduction of nitrate to ammonia, Nat. Commun. 15 (2024) 8583.
[6] M. Jiang, L. Han, P. Peng, Y. Hu, Y. Xiong, C. Mi, Z. Tie, Z. Xiang, Z. Jin, Quasi-phthalocyanine conjugated covalent organic frameworks with nitrogen-coordinated transition metal centers for high-efficiency electrocatalytic ammonia synthesis, Nano Lett. 22 (2021) 372–379.
[7] M. Jiang, J. Su, X. Song, P. Zhang, M. Zhu, L. Qin, Z. Tie, J.-L. Zuo, Z. Jin, Interfacial reduction nucleation of noble metal nanodots on redox-active metal-organic frameworks for high-efficiency electrocatalytic conversion of nitrate to ammonia, Nano Lett. 22 (2022) 2529–2537.
[8] X. Zhou, W. Xu, Y. Liang, H. Jiang, Z. Li, S. Wu, Z. Gao, Z. Cui, S. Zhu, Dynamically restructuring nanoporous cu-co electrocatalyst for efficient nitrate electroreduction to ammonia, ACS Catal. 14 (2024) 12251–12259.
[9] X. Chen, G. Ren, Y. Wang, Z. Li, Z. Zhang, X. Meng, Introduction of element Bi in the P-block promotes $N_2$ activation for efficient electrocatalytic nitrogen reduction to produce ammonia, Appl. Catal. B Environ. Energy 355 (2024) 124173.
[10] M. Jiang, X. Chen, F. Chen, M. Wang, X. Luo, Y. He, C. Wu, L. Zhang, X. Li, X. Liao, Z. Jiang, Z. Jin, Effective $N_2$ activation strategies for electrochemical ammonia synthesis, Chem 11 (2025) 102441.
[11] X. Zhao, Y. Jiang, M. Wang, Y. Huan, Q. Cheng, Y. He, T. Qian, C. Yan, Comprehensive understanding of the thriving electrocatalytic nitrate/nitrite reduction to ammonia under ambient conditions, J. Energy Chem. 92 (2024) 459–483.
[12] S. Ye, Z. Chen, G. Zhang, W. Chen, C. Peng, X. Yang, L. Zheng, Y. Li, X. Ren, H. Cao, D. Xue, J. Qiu, Q. Zhang, J. Liu, Elucidating the activity, mechanism and application of selective electrosynthesis of ammonia from nitrate on cobalt phosphide, Energy Environ. Sci. 15 (2022) 760–770.
[13] M. Jiang, X. Huang, D. Luo, C. Tian, Z. Jin, Recent breakthroughs in electrocatalytic reduction of nitrogen-oxyanions for environmentally benign ammonia synthesis, Nano Energy 135 (2025) 110683.
[14] F. Chen, X. Zhou, H. Wang, X. Liu, Q. Yang, X. Chen, Q. Mu, J. Liu, X. Li, X. Liao, Z. Jiang, Z. Jin, M. Jiang, Bidirectional nitrogen neutralization via coupled electrocatalytic processes of nitrate reduction and hydrazine oxidation, Adv. Funct. Mater. 35 (2025) 2421405.
[15] Y. Xiao, X. Tan, B. Du, Y. Guo, W. He, H. Cui, C. Wang, Strained Au skin on mesoporous intermetallic $AuCu_3$ nanocoral for electrocatalytic conversion of nitrate to ammonia across a wide concentration range, Angew. Chem. Int. Ed. 63 (2024) e202408758.
[16] P.H. van Langevelde, I. Katsounaros, M.T.M. Koper, Electrocatalytic nitrate reduction for sustainable ammonia production, Joule 5 (2021) 290–294.
[17] Y. Wang, W. Zhou, R. Jia, Y. Yu, B. Zhang, Unveiling the activity origin of a copper-based electrocatalyst for selective nitrate reduction to ammonia, Angew. Chem. Int. Ed. 59 (2020) 5350–5354.
[18] M. Jiang, J. Su, X. Song, P. Zhang, M. Zhu, L. Qin, Z. Tie, J.-L. Zuo, Z. Jin, Interfacial reduction nucleation of noble metal nanodots on redox-active metal-organic frameworks for high-efficiency electrocatalytic conversion of nitrate to ammonia, Nano Lett. 22 (2022) 2529–2537.
[19] X.-Y. Ji, K. Sun, Z.-K. Liu, X. Liu, W. Dong, X. Zuo, R. Shao, J. Tao, Identification of dynamic active sites among cu species derived from MOFs@CuPc for electrocatalytic nitrate reduction reaction to ammonia, Nano Micro Lett. 15 (2023) 110.
[20] L.-Y. Zhang, W. Shang, S. Qiao, W. Liu, Y. Shi, Porous $Cu_1/TiO_{2-X}$ catalytic binding pocket for near-unity nitrate-to-ammonia conversion, ACS Catal. 14 (2024) 15827–15836.

[21] P. Li, Z. Jin, Z. Fang, G. Yu, A single-site iron catalyst with preoccupied active centers that achieves selective ammonia electrosynthesis from nitrate, Energy Environ. Sci. 14 (2021) 3522–3531.

[22] Z. Zhang, X. Feng, Z. Zhang, L. Chen, W. Liu, L. Tong, X. Gao, J. Zhang, Graphdiyne enabled nitrogen vacancy formation in copper nitride for efficient ammonia synthesis, J. Am. Chem. Soc. 146 (2024) 14898–14904.

[23] Q. Cheng, S. Liu, Y. He, M. Wang, H. Ji, Y. Huan, T. Qian, C. Yan, J. Lu, Multivariate covalent organic frameworks with tailored electrostatic potential promote nitrate electroreduction to ammonia in acid, Nat. Commun. 16 (2025) 3717.

[24] M. Jiang, Q. Zhu, X. Song, Y. Gu, P. Zhang, C. Li, J. Cui, J. Ma, Z. Tie, Z. Jin, Batch-scale synthesis of nanoparticle-agminated three-dimensional porous cu@$Cu_2O$ microspheres for highly selective electrocatalysis of nitrate to ammonia, Environ. Sci. Technol. 56 (2022) 10299–10307.

[25] J. Wang, J. Cai, K.-X. Ren, L. Liu, S.-J. Zheng, Z.-Y. Wang, S.-Q. Zang, Stepwise structural evolution toward robust carboranealkynyl-protected copper nanocluster catalysts for nitrate electroreduction, Sci. Adv. 10 (2024) eadn7556.

[26] X. Chen, F. Chen, X. Zhong, J. Ding, H. Wang, L. Dai, X. Ma, H. Wang, C. Wu, X. Li, Y. Xiong, Z. Jin, M. Jiang, Copper nanoclusters featuring fully inorganic anionic ligands for enhanced electrocatalytic nitrate-to-ammonia conversion, J. Energy Chem. 110 (2025) 768–777.

[27] J. Liang, Z. Li, L. Zhang, X. He, Y. Luo, D. Zheng, Y. Wang, T. Li, H. Yan, B. Ying, S. Sun, Q. Liu, M.S. Hamdy, B. Tang, X. Sun, Advances in ammonia electrosynthesis from ambient nitrate/nitrite reduction, Chem 9 (2023) 1768–1827.

[28] G.-F. Chen, Y. Yuan, H. Jiang, S.-Y. Ren, L.-X. Ding, L. Ma, T. Wu, J. Lu, H. Wang, Electrochemical reduction of nitrate to ammonia via direct eight-electron transfer using a copper-molecular solid catalyst, Nat. Energy 5 (2020) 605–613.

[29] Y. Wang, L. Zhang, Y. Niu, D. Fang, J. Wang, Q. Su, C. Wang, Boosting $NH_3$ production from nitrate electroreduction via electronic structure engineering of $Fe_3C$ nanoflakes, Green Chem. 23 (2021) 7594–7608.

[30] H. Li, S. Li, R. Guan, Z. Jin, D. Xiao, Y. Guo, P. Li, Modulating the surface concentration and lifetime of active hydrogen in cu-based layered double hydroxides for electrocatalytic nitrate reduction to ammonia, ACS Catal. 14 (2024) 12042–12050.

[31] M. Luo, Z. Wang, Y.C. Li, J. Li, F. Li, Y. Lum, D.-H. Nam, B. Chen, J. Wicks, A. Xu, T. Zhuang, W.R. Leow, X. Wang, C.-T. Dinh, Y. Wang, Y. Wang, D. Sinton, E. H. Sargent, Hydroxide promotes carbon dioxide electroreduction to ethanol on copper via tuning of adsorbed hydrogen, Nat. Commun. 10 (2019) 5814.

[32] M. Xu, M. Wei, Layered double hydroxide-based catalysts: recent advances in preparation, structure, and applications, Adv. Funct. Mater. 28 (2018) 1802943.

[33] T. Hu, Z. Gu, G.R. Williams, M. Strimaite, J. Zha, Z. Zhou, X. Zhang, C. Tan, R. Liang, Layered double hydroxide-based nanomaterials for biomedical applications, Chem. Soc. Rev. 51 (2022) 6126–6176.

[34] X. Ma, J. Zhong, W. Huang, R. Wang, S. Li, Z. Zhou, C. Li, Tuning the d-band centers of bimetallic FeNi catalysts derived from layered double hydroxides for selective electrocatalytic reduction of nitrates, Chem. Eng. J. 474 (2023) 145721.

[35] Z. Chen, X. Wang, Z. Han, S. Zhang, S. Pollastri, Q. Fan, Z. Qu, D. Sarker, C. Scheu, M. Huang, H. Cölfen, Revealing the formation mechanism and optimizing the synthesis conditions of layered double hydroxides for the oxygen evolution reaction, Angew. Chem. Int. Ed. 62 (2023) e202215728.

[36] Y. Jiang, W. Cheng, J.-L. Chen, Y. Liu, L. Liu, Z. Xu, N. Ma, R.Y.-Y. Lin, L. Ren, C. Meng, Facile synthesis of dual-MOF ultrathin nanosheets supported on layered double hydroxides heterostructure: electron modulation strategy for enhanced electrocatalytic water splitting, Appl. Catal. B Environ. 361 (2025) 124662.

[37] T. Hui, H. Liu, T. Li, J. Pan, T. Zheng, R. Zhang, X. Meng, H. Liu, Z. Liu, C. Xu, Efficient electrooxidation of 5-hydroxymethylfurfural via phosphate intercalated hydroxides: a dual-cycle mechanism, Appl. Catal. B Environ. 355 (2024) 124147.

[38] H. Li, Q. Yu, X. Zhu, H. Wu, Z. Dai, L. Li, W. Zhu, S. Li, Z. Chen, V-doping and cation-vacancy engineering synergistically promote the electrocatalysis ability of NiFe-layered double hydroxides towards the oxygen evolution and urea oxidation reactions, Chem. Eng. J. 493 (2024) 152860.

[39] S. Wang, K. Ge, H. Cui, S. Li, Y. Yang, M. Pan, L. Zhu, Self-polarization-enhanced oxygen evolution reaction by flower-like core-shell $BaTiO_3$@NiFe-layered double hydroxide heterojunctions, Chem. Eng. J. 479 (2024) 147831.

[40] X. Han, Z. Liu, M. Cao, H. Ren, C. Du, F. Yang, B. Shan, R. Chen, Atomic layer infiltration enabled cu coordination environment construction for enhanced electrochemical $CO_2$ reduction selectivity: case study of a cu metal-organic framework, Chem. Mater. 34 (2022) 6713–6722.

[41] D. Sun, L. Chen, L. Zeng, X. Shi, J. Lu, Quasi-cu-MOFs: highly improved water stability and electrocatalytic activity toward $H_2O_2$ reduction among pristine 3D MOFs, J Mater Chem A 11 (2023) 31–40.

[42] C.F. Wen, S. Yang, J.J. He, Q. Niu, P.F. Liu, H.G. Yang, Anionic metal-organic framework derived cu catalyst for selective $CO_2$ electroreduction to hydrocarbons, Small 20 (2024) 2405051.

[43] X. Lin, Z. Wang, S. Cao, Y. Hu, S. Liu, X. Chen, H. Chen, X. Zhang, S. Wei, H. Xu, Z. Cheng, Q. Hou, D. Sun, X. Lu, Bioinspired trimesic acid anchored electrocatalysts with unique static and dynamic compatibility for enhanced water oxidation, Nat. Commun. 14 (2023) 6714.

[44] J. Chen, Z. Li, Z. Li, Y. Zhou, Y. Lai, Lattice-matched spinel/layered double hydroxide 2D/2D heterojunction towards large-current-density overall water splitting, Appl. Catal. B Environ. 355 (2024) 124204.

[45] S. Liu, S. Dou, J. Meng, Y. Liu, Y. Liu, H. Yu, Efficient biobased carboxylic acids synthesis by synergistic electrocatalysis of multi-active sites on bimetallic cu-co oxide/oxyhydroxide, Appl Catal B 331 (2023) 122709.

[46] M. Zhen, X. Meng, X. Wang, Z. Zhang, S.-Q. Guo, Z. Hu, B. Shen, Layered double hydroxides-MXene heterointerfaces with abundant anion vacancies expediting sulfur redox kinetics for high-performance lithium-sulfur batteries, Chem. Eng. J. 489 (2024) 151285.

[47] Y. Wang, Y. Liu, S. Liu, Y. Qin, J. Liu, X. Jia, Q. Jiang, X. Wang, Y. Zhao, L. Liu, H. Liu, H. Zhao, Y. Jiang, D. Liang, H. Wu, B. Jia, X. Qu, H. Li, M. Qin, Gd-induced oxygen vacancy creation activates lattice oxygen oxidation for water electrolysis, Adv. Funct. Mater. 35 (2025) 2500118.

[48] X. Bai, J. Yang, D. Mantzavinos, A. Katsaounis, H. Zhang, F. Zhang, F. Sun, C. Pan, H. Di, Z. Jiang, Simultaneous dehalogenation and oxidation of dichloroacetamide by cu-modified CoFe-LDH in three-dimensional continuous flow aerated electrocatalytic reactor, Chem. Eng. J. 500 (2024) 156652.

[49] V.V. Burungale, H. Bae, M.A. Gaikwad, P. Mane, J. Heo, C. Seong, S.-H. Kang, S.-W. Ryu, J.-S. Ha, $Cu_2O$-based trifunctional catalyst for enhanced alkaline water splitting and hydrazine oxidation: integrating sulfurization, co incorporation, and LDH heterostructure, Chem. Eng. J. 486 (2024) 150175.

[50] X. Xia, S. Wang, D. Liu, F. Wang, X. Zhang, H. Zhang, X. Yu, Z. Pang, G. Li, C. Chen, Y. Zhao, L. Ji, Q. Xu, X. Zou, X. Lu, Electronic modulation in cu doped NiCo LDH/NiCo heterostructure for highly efficient overall water splitting, Small 20 (2024) 2311182.

[51] D.K. Cho, H.W. Lim, A. Haryanto, B. Yan, C.W. Lee, J.Y. Kim, Intercalation-induced irreversible lattice distortion in layered double hydroxides, ACS Nano 18 (2024) 20459–20467.

[52] H. Xu, G. Xin, W. Hu, Z. Zhang, C. Si, J. Chen, L. Lu, Y. Peng, X. Li, Single-atoms Ru/NiFe layered double hydroxide electrocatalyst: efficient for oxidation of selective oxidation of 5-hydroxymethylfurfural and oxygen evolution reaction, Appl Catal B 339 (2023) 123157.

[53] M. Jiang, M. Zhu, J. Ding, H. Wang, Q. Yu, X. Chen, Y. He, M. Wang, X. Luo, C. Wu, L. Zhang, X. Yao, H. Wang, X. Li, X. Liao, Z. Jiang, Z. Jin, Nanocluster-agminated amorphous cobalt nanofilms for highly selective electroreduction of nitrate to ammonia, J. Hazard. Mater. 476 (2024) 134909.

[54] M. Wang, S. Li, Y. Gu, W. Xu, H. Wang, J. Sun, S. Chen, Z. Tie, J.-L. Zuo, J. Ma, J. Su, Z. Jin, Polynuclear cobalt cluster-based coordination polymers for efficient nitrate-to-ammonia electroreduction, J. Am. Chem. Soc. 146 (2024) 20439–20448.

[55] J.-J. Zhang, Y.-Y. Lou, Z. Wu, X.J. Huang, S.-G. Sun, Spatially separated cu/Ru on ordered mesoporous carbon for superior ammonia electrosynthesis from nitrate over a wide potential window, J. Am. Chem. Soc. 146 (2024) 24966–24977.

[56] X.H. Wang, Q.L. Hong, L.Y. Shao, Q.G. Zhai, Y.C. Jiang, X. Ai, Y. Chen, S.N. Li, Copper-nickel oxide nanosheets with atomic thickness for high-efficiency sulfur ion electrooxidation assisted nitrate electroreduction to ammonia, Adv. Funct. Mater. 34 (2024) 2408834.

[57] J. Yu, R.-T. Gao, X. Guo, N.T. Nguyen, L. Wu, L. Wang, Electrochemical nitrate reduction to ammonia on AuCu single-atom alloy aerogels under wide potential window, Angew. Chem. Int. Ed. 64 (2024) e202415975.

[58] K. Liu, H. Li, M. Xie, P. Wang, Z. Jin, Y. Liu, M. Zhou, P. Li, G. Yu, Thermally enhanced relay electrocatalysis of nitrate-to-ammonia reduction over single-atom-alloy oxides, J. Am. Chem. Soc. 146 (2024) 7779–7790.

[59] X. Sun, Y. He, M. Wang, Q. Cheng, Y. Huan, S. Liu, J. Liu, T. Qian, C. Yan, J. Lu, Maximizing available active hydrogen on FeNi substitutional solid-solution alloy to boost electrosynthesis of ammonia from nitrate, ACS Nano 19 (2025) 8189–8199.

[60] J. Zhou, Y. Wang, D. Wu, Y. Wang, T. Zhou, T.X. Liu, M. Wen, Y. Fu, Reconstructing active sites in Ni-Co double hydroxides to enhance electrocatalytic efficiency for nitrate reduction to ammonia, J. Energy Chem. 110 (2025) 133–142.

[61] Y. Chen, Y. Bai, Z. Fang, K. Jia, X. Jiang, J. Li, W. Fan, Synergistic cobalt valence cycling and oxygen vacancy in co(II)co(III)Al(III)-layered double hydroxides enable efficient electrocatalytic nitrate-to-ammonia conversion, Surf Interfaces 72 (2025) 107105.